

## Photoelectrocatalysts

# Hierarchical MoS<sub>2</sub>@TiO<sub>2</sub> Heterojunctions for Enhanced Photocatalytic Performance and Electrocatalytic Hydrogen Evolution

Yu Dong,<sup>[a]</sup> Sheng-You Chen,<sup>[a]</sup> Yi Lu,<sup>[a]</sup> Yu-Xuan Xiao,<sup>[a]</sup> Jie Hu,<sup>[a]</sup> Si-Ming Wu,<sup>[a]</sup> Zhao Deng,<sup>\*,[a]</sup> Ge Tian,<sup>\*,[a]</sup> Gang-Gang Chang,<sup>[a]</sup> Jing Li,<sup>[b]</sup> Silvia Lenaerts,<sup>[c]</sup> Christoph Janiak,<sup>[d]</sup> Xiao-Yu Yang,<sup>\*,[a]</sup> and Bao-Lian Su<sup>[a, e]</sup>

**Abstract:** Hierarchical MoS<sub>2</sub>@TiO<sub>2</sub> heterojunctions were synthesized through a one-step hydrothermal method by using protonic titanate nanosheets as the precursor. The TiO<sub>2</sub> nanosheets prevent the aggregation of MoS<sub>2</sub> and promote the carrier transfer efficiency, and thus enhance the photocatalytic and electrocatalytic activity of the nanostructured MoS<sub>2</sub>. The obtained MoS<sub>2</sub>@TiO<sub>2</sub> has significantly enhanced photocatalytic activity in the degradation of rhodamine B

(over 5.2 times compared with pure MoS<sub>2</sub>) and acetone (over 2.8 times compared with pure MoS<sub>2</sub>). MoS<sub>2</sub>@TiO<sub>2</sub> is also beneficial for electrocatalytic hydrogen evolution (26 times compared with pure MoS<sub>2</sub>, based on the cathodic current density). This work offers a promising way to prevent the self-aggregation of MoS<sub>2</sub> and provides a new insight for the design of heterojunctions for materials with lattice mismatches.

## Introduction

MoS<sub>2</sub> has become a promising candidate in photocatalysis, energy storage, and optoelectronic devices due to its graphite-analogous structure and corresponding graphene-like properties.<sup>[1–3]</sup> However, its great tendency to form irregular aggregates with multi-layered stacks greatly reduces the specific surface, blocks the active edge sites, and impedes carrier transfer.<sup>[4]</sup> An efficient strategy to address these issues is the use of nanocomposites, in which a foreign nanostructure is used to separate the MoS<sub>2</sub> layers, combine multiple functionalities, and form an intimate nano/atomic interface.<sup>[5–9]</sup> TiO<sub>2</sub>, with excellent chemical stability, is the most used n-type semiconductor and has been widely used in MoS<sub>2</sub>/TiO<sub>2</sub> p–n heterojunction nano-

composites to enhance mass/charge transport and the structural stability of MoS<sub>2</sub>.<sup>[10–14]</sup> Post-synthesis is often chosen as the rational design, for example, TiO<sub>2</sub> nanoparticles doped on thin-layer MoS<sub>2</sub>,<sup>[15]</sup> MoS<sub>2</sub> nanosheets intersected on/in TiO<sub>2</sub> nanorods,<sup>[11]</sup> or MoS<sub>2</sub> particles supported on TiO<sub>2</sub> nanoarrays.<sup>[16]</sup> Notably, it is not easy to obtain the perfect heterojunction growth of MoS<sub>2</sub>/TiO<sub>2</sub> structures due to matching constraints, such as lattice constants and atomic arrangement.<sup>[7,17]</sup> A direct hydrothermal transformation by using nanostructured Ti sources, such as NH<sub>2</sub>-MIL-125(Ti) nanocrystals<sup>[18]</sup> and unilamellar Ti<sub>0.87</sub>O<sub>2</sub> nanosheets,<sup>[17]</sup> has been recently developed for various heterostructures. The MoS<sub>2</sub>/TiO<sub>2</sub> nanointerface fusion<sup>[19]</sup> in layer-by-layer and core–shell structures not only enhances the

[a] Y. Dong, S.-Y. Chen, Y. Lu, Y.-X. Xiao, J. Hu, S.-M. Wu, Dr. Z. Deng, Prof. G. Tian, Prof. G.-G. Chang, Prof. X.-Y. Yang, Prof. B.-L. Su  
State Key Laboratory Advanced Technology for Materials Synthesis and Processing and School of Materials Science and Engineering  
Wuhan University of Technology  
122 Luoshi Road  
Wuhan, 430070 (China)  
E-mail: dengzhao@whut.edu.cn  
tiange@whut.edu.cn  
xyyang@whut.edu.cn

[b] Prof. J. Li  
The State Key Laboratory of Solid Lubrication  
Lanzhou Institute of Chemical Physics  
Chinese Academy of Sciences  
Lanzhou 730000 (China)

[c] Prof. S. Lenaerts  
Research Group of Sustainable Energy and Air Purification (DuEL), Department of Bioscience Engineering

University of Antwerp  
Antwerp (Belgium)

[d] Prof. C. Janiak  
Institut für Anorganische Chemie und Strukturchemie  
Heinrich-Heine-Universität Düsseldorf  
40204 Düsseldorf (Germany)

[e] Prof. B.-L. Su  
Laboratory of Inorganic Materials Chemistry (CMI)  
University of Namur  
61 rue de Bruxelles  
5000 Namur (Belgium)

Supporting information and the ORCID identification number(s) for the author(s) of this article can be found under:  
<https://doi.org/10.1002/asia.201800359>

photoelectrocatalyst performance but also provides the MoS<sub>2</sub> with highly structural stability.

Protonic titanate nanosheets (TN) have a very thin nanostructure and thus it is easy to adjust their charge,<sup>[20]</sup> which could provide nucleation sites for the growth of MoS<sub>2</sub> nanosheets through electrostatic self-assembly. Very interestingly, the layers of TN split during the transformation to anatase because of structural changes and atom rearrangement during the hydrothermal process.<sup>[21,22]</sup> This unique phenomenon could avoid the self-aggregation of large-sized layers, and the TiO<sub>2</sub> nanosheets can be uniformly loaded and intimately composited with MoS<sub>2</sub> nanosheets. Moreover, the exfoliation of titanate nanolayers in the solid-state synthesis and osmotic swelling offers an ecologically benign and low-cost approach to scale up the high-performance photoelectrocatalysts.<sup>[23]</sup> Herein, we employed TN as the TiO<sub>2</sub> nanosheet precursor and used a one-step hydrothermal method to synthesize hierarchical MoS<sub>2</sub>@TiO<sub>2</sub> heterojunctions. The TiO<sub>2</sub>-nanosheets-loaded hierarchical flower-like MoS<sub>2</sub> structure can prevent the aggregation of MoS<sub>2</sub> and enhance the carrier transfer efficiency. The heterostructures exhibit superior performance compared with pure MoS<sub>2</sub> in photocatalytic activity and electrocatalytic hydrogen evolution, and high structural stability.

## Results and Discussion

Figure 1 presents the synthesis process and formation mechanism of MoS<sub>2</sub>@TiO<sub>2</sub>. After mixing of the TN, Mo, and S precursors (Figure 1a), surface adsorption onto the protonic titanate nanosheets occurs by electrostatic attraction and the assembly

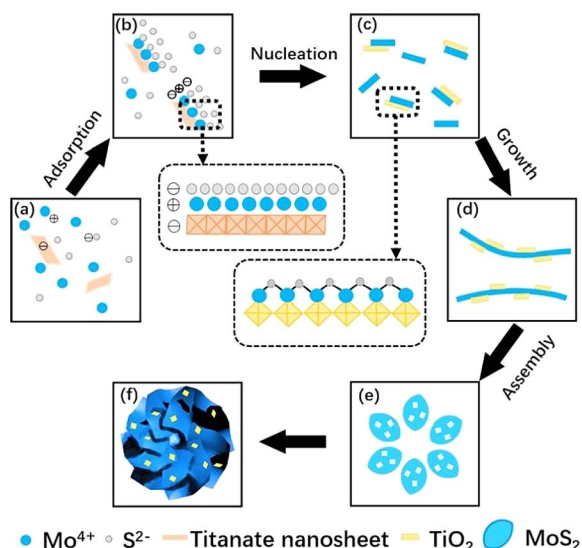


**Figure 1.** Schematic representation of the formation mechanism of MoS<sub>2</sub>@TiO<sub>2</sub>: a) protonic titanate nanosheets (TN) with negatively charged surfaces in a solution that contained a Mo source and an S source; b) Mo<sup>4+</sup> ions are adsorbed onto the TN, and S<sup>2-</sup> ions are attracted by Mo<sup>4+</sup> to form an electronic triple layer (enlargement); c) TN is converted to TiO<sub>2</sub> during the hydrothermal process, MoS<sub>2</sub> grains nucleate on the TiO<sub>2</sub> and form intimate interfaces between MoS<sub>2</sub> and TiO<sub>2</sub> (enlargement); d) the growth of MoS<sub>2</sub> nanosheets; e) self-assembly of MoS<sub>2</sub>@TiO<sub>2</sub> layers; f) the corresponding 3D model.

of negative–positive–negative electric triple layers (Figure 1b and enlargement),<sup>[19,24,25]</sup> formed by the negative charges caused by Ti vacancies in the TN, the Mo<sup>4+</sup> ions, and the S<sup>2-</sup> ions. During the hydrothermal process, MoS<sub>2</sub> layers nucleate (Figure 1c), grow (Figure 1d), and assemble (Figure 1e). The MoS<sub>2</sub> first tends to nucleate and grow along the negatively charged TN, and the existence of TN restrains the irregular aggregation of MoS<sub>2</sub>. MoS<sub>2</sub> grows and form larger sheets, whereas the TN is transformed into anatase TiO<sub>2</sub> and splits into small-sized nanosheets in the dehydration reaction. Therefore, the MoS<sub>2</sub> layers support the TiO<sub>2</sub> nanosheets instead. Typically, with transformation from the TN to TiO<sub>2</sub>, intimate interfaces form between MoS<sub>2</sub> and TiO<sub>2</sub> (Figure 1c and enlargement). Finally, hierarchically structured MoS<sub>2</sub>@TiO<sub>2</sub> heterojunctions (Figure 1e and f) are obtained through the self-assembly of MoS<sub>2</sub>@TiO<sub>2</sub> nanosheets.

The morphology of MoS<sub>2</sub>@TiO<sub>2</sub> heterojunctions is shown in Figure 2. MoS<sub>2</sub>@TiO<sub>2</sub> heterojunctions have a hierarchical flower-like structure. In contrast, pure MoS<sub>2</sub> nanosheets tend to aggregate into microspheres (Figure S1), which thus block the active edge sites. In Figure 2b, it is obvious that MoS<sub>2</sub>@TiO<sub>2</sub> is constructed by MoS<sub>2</sub> layers with TiO<sub>2</sub> nanosheets evenly dispersed on the surface of MoS<sub>2</sub>, which is consistent with the SAED pattern (Figure 2b, inset). The HR-TEM image in Figure 2c presents the heterojunction structure in region I of Figure 2b. The lattice fringes of 0.35 nm agree with the anatase titania (101) interplanar spacing, whereas the 0.6 nm fringes correspond to the (002) planes of MoS<sub>2</sub> nanosheets. It is obvious that TiO<sub>2</sub> and MoS<sub>2</sub> are clearly crystalline and form heterojunction structures. In the corresponding inverse FFT image (Figure 2d) of region II (in Figure 2c), between TiO<sub>2</sub> and MoS<sub>2</sub> the crystal fusion domain shows a disordered atomic arrangement and strong lattice distortions at the phase edge. This unique fused structure improves the photogenerated charge carrier

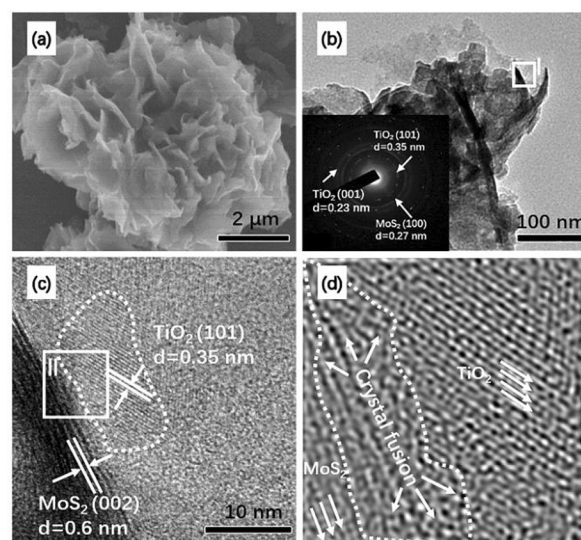


**Figure 2.** a) SEM image, b) TEM image, and inset: SAED pattern of MoS<sub>2</sub>@TiO<sub>2</sub> heterojunctions. c) HR-TEM image of region I and d) inverse FFT image of region II, which shows the crystal fusion region between TiO<sub>2</sub> and MoS<sub>2</sub>.

transfer and significantly increases the number of catalytically active sites due to very low interface losses during electron transmission.<sup>[19]</sup> This structure formation may be attributed to the nucleation of MoS<sub>2</sub> onto the TN surface based on electrostatic adsorption and atom rearrangements during the hydrothermal process. These nanofused domains facilitate the separation of carriers, bond the different nanoparticles, and enhance the stability of the nanostructure.<sup>[26]</sup> Interestingly, compared with the protonic titanate nanosheets, the TiO<sub>2</sub> nanosheets have a much smaller size (around 20 nm), which results from a dissolution reaction during the hydrothermal process (Figure S2). The decrease in the size of the TiO<sub>2</sub> nanosheets increases the dispersion of TiO<sub>2</sub>, which makes it uniformly loaded and thus forms an intimate composite of MoS<sub>2</sub>@TiO<sub>2</sub>. To illustrate the distribution of TiO<sub>2</sub>, EDS analysis was performed in combination with SEM. The element mapping images of Ti, Mo, and S indicate that the TiO<sub>2</sub> is uniformly dispersed on MoS<sub>2</sub> (Figure S3).

The structure of MoS<sub>2</sub>@TiO<sub>2</sub> was characterized by using XRD and N<sub>2</sub> adsorption-desorption isotherms. The XRD patterns of protonic titanate (HTO), pure MoS<sub>2</sub> nanosheets, MoS<sub>2</sub>@TiO<sub>2</sub>, and TN after hydrothermal treatment (denoted as TiO<sub>2</sub>) are shown in Figure S4. In the pure MoS<sub>2</sub> sample, the detected peaks can be assigned to the (002), (100), (101), (102), (103), and (006) planes in the hexagonal phase (ICDD card no. 37-1492). The diffraction peak of HTO was as reported before.<sup>[20]</sup> After the exfoliation and hydrothermal treatment of HTO, it was converted into anatase TiO<sub>2</sub> (ICDD card no. 21-1272), which may be attributed to the dehydration reaction.<sup>[21,22]</sup> For MoS<sub>2</sub>@TiO<sub>2</sub>, the peaks at around 25.3 ((101) plane) and 48.1° ((200) plane) are attributed to anatase TiO<sub>2</sub>, and the others are consistent with MoS<sub>2</sub>. We analyzed the surface area by using nitrogen adsorption-desorption isotherms (Figure S5). The specific surface area of MoS<sub>2</sub>@TiO<sub>2</sub> is about three times that of pure MoS<sub>2</sub>. This will promote the exposure of more active sites, increase the contact areas during the reaction, and thus improve the photocatalytic activity.<sup>[27,28]</sup>

To investigate the photocatalytic properties of MoS<sub>2</sub>@TiO<sub>2</sub>, the samples were irradiated under visible light to degrade Rhodamine B (RhB). A comparison of the degradation performance of MoS<sub>2</sub>@TiO<sub>2</sub> samples (final weight ratios of TiO<sub>2</sub>/MoS<sub>2</sub> were 0.02, 0.11, and 0.75 from the ICP results (Table S1)) are shown in Figure S6. MoS<sub>2</sub>@TiO<sub>2</sub> samples and pure MoS<sub>2</sub> exhibited high adsorption of the dye molecules compared with TiO<sub>2</sub>. After visible-light irradiation, the performance was promoted for the heterojunctions and the photocatalytic rate of MoS<sub>2</sub>@TiO<sub>2</sub>-0.11 is about 5.2 times that of pure MoS<sub>2</sub>. Pure TiO<sub>2</sub> and commercial P25 showed negligible photocatalytic activity because they cannot absorb visible light (Figure S7). Sample MoS<sub>2</sub>@TiO<sub>2</sub>-0.11 showed superior photocatalytic properties and the degradation rate was 2.1 and 3.3 times that of MoS<sub>2</sub>@TiO<sub>2</sub>-0.02 and MoS<sub>2</sub>@TiO<sub>2</sub>-0.75, respectively. A small loading of TiO<sub>2</sub> can hardly improve the multiple stacks of MoS<sub>2</sub> (Figure S1), whereas overloading with TiO<sub>2</sub> would hinder the absorption of visible light. The physically mixed MoS<sub>2</sub> and TiO<sub>2</sub> showed quite low photocatalytic activity, which indicates that the nanofused interface of MoS<sub>2</sub> and TiO<sub>2</sub> plays an important role in the photo-

catalytic activity. To probe the durability of MoS<sub>2</sub>@TiO<sub>2</sub> for degradation, we conducted cycling experiments with MoS<sub>2</sub>@TiO<sub>2</sub>-0.11, and the degradation rate remained stable after five cycles and retained over 88% ( $\pm 2\%$ ) of the initial activity (Figure 3b). In the degradation of volatile organic compounds (acetone; see Figure 3a), MoS<sub>2</sub>@TiO<sub>2</sub> showed the highest photocatalytic activity and its apparent rate constant (*k*) reached  $10.1 \times 10^{-3} \text{ min}^{-1}$ , which is about 2.8 times that of pure MoS<sub>2</sub>.

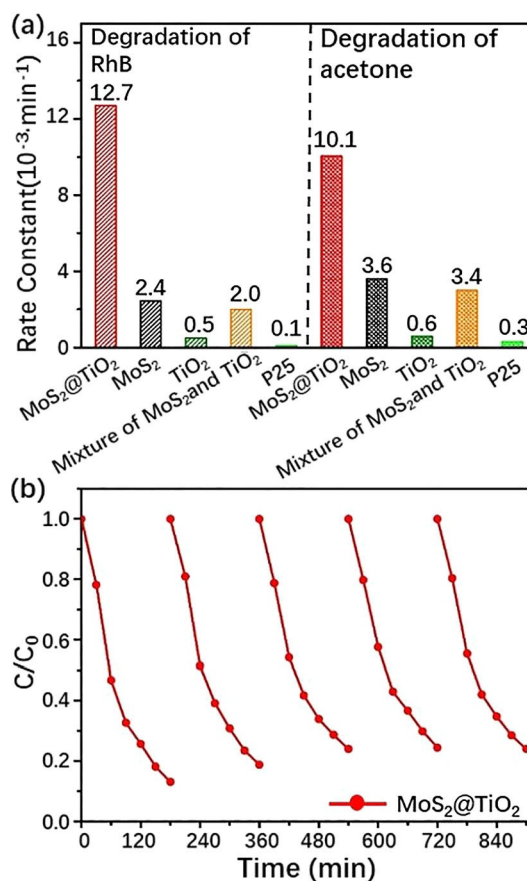


**Figure 3.** a) Photocatalytic rate constant for the RhB and acetone degradation reactions with the MoS<sub>2</sub>@TiO<sub>2</sub>, MoS<sub>2</sub>, MoS<sub>2</sub> and TiO<sub>2</sub> mixture, TiO<sub>2</sub>, and P25 catalysts under visible-light irradiation; b) cycle performance of MoS<sub>2</sub>@TiO<sub>2</sub> in the RhB degradation reaction under visible light.

Figure 4a and b display the electrochemical properties of the samples. TiO<sub>2</sub> exhibited a large onset overpotential of 340 mV for the hydrogen evolution reaction (HER) because of poor intrinsic conductivity, whereas for pure MoS<sub>2</sub> the onset overpotential was 230 mV. Our MoS<sub>2</sub>@TiO<sub>2</sub> heterojunction compound showed a decreased onset potential with a value of about 130 mV, which suggests good catalytic activity of the product. Moreover, the MoS<sub>2</sub>@TiO<sub>2</sub> heterojunctions displayed the largest cathodic current density of all the tested samples, 31.3 mA cm<sup>-2</sup> at an overpotential of 200 mV, which is about 26 times that of pure MoS<sub>2</sub>. Because the cathodic current density is proportional to the quantity of evolved hydrogen, MoS<sub>2</sub>@TiO<sub>2</sub> exhibits prominent hydrogen evolution behavior. In Figure 4b, the Tafel slope of MoS<sub>2</sub>@TiO<sub>2</sub> is about 80 mV dec<sup>-1</sup>,

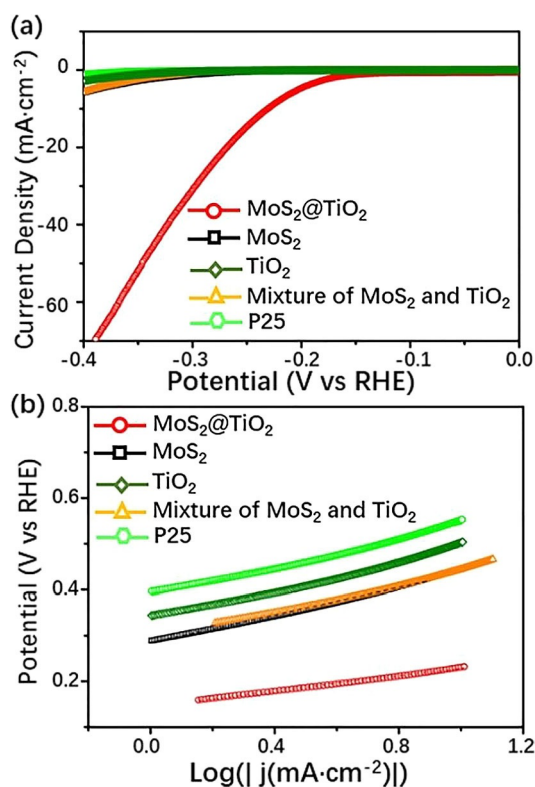


**Figure 4.** a) Polarization curves and b) the corresponding Tafel plots for  $\text{MoS}_2@\text{TiO}_2$ ,  $\text{TiO}_2$ , P25,  $\text{MoS}_2$ , and a mixture of  $\text{MoS}_2$  and  $\text{TiO}_2$ .

much lower than that of pure  $\text{MoS}_2$  ( $144 \text{ mV dec}^{-1}$ ). The small Tafel slope is advantageous for practical applications because it will lead to a faster increment of HER rate at increased overpotentials.<sup>[29]</sup> The Tafel slope comparison confirmed that the HER performance of  $\text{MoS}_2@\text{TiO}_2$  is better than that of pure  $\text{MoS}_2$  and commercial P25 catalyst. The durability of  $\text{MoS}_2@\text{TiO}_2$  and  $\text{MoS}_2$  was tested at static cathodic current (1.96 mA) for 10 h. As shown in Figure S8, the overpotential of  $\text{MoS}_2@\text{TiO}_2$  only increased by 24 mV, whereas for  $\text{MoS}_2$ , the value increased by 50 mV, which indicates that  $\text{MoS}_2@\text{TiO}_2$  has superior stability in long-term electrochemical processes.

X-ray photoelectron spectroscopy (XPS) was used to investigate the chemical states of Mo, S, and Ti in the  $\text{MoS}_2@\text{TiO}_2$  heterostructures (Figure 5a,b and Figure S9). The high-resolution XPS curves indicate that the peaks at 233.1 and 229.9 eV for pure  $\text{MoS}_2$  can be assigned to  $\text{Mo}3d_{3/2}$  and  $\text{Mo}3d_{5/2}$ , respectively, in the +4 oxidation state. The binding energy of Mo and S in  $\text{MoS}_2@\text{TiO}_2$  were both shifted by about 0.3 eV in the lower energy direction. The Ti peaks located at 464.1 and 458.4 eV represent  $\text{Ti}2p_{1/2}$  and  $\text{Ti}2p_{3/2}$ , respectively, and indicate an oxidation state of  $\text{Ti}^{4+}$ . For  $\text{MoS}_2@\text{TiO}_2$  the  $\text{Ti}2p_{1/2}$  and  $\text{Ti}2p_{3/2}$  peaks were shifted to 465.5 and 459.6 eV. The shift in the peaks indicates a possible new bond, Ti-O-Mo, and an interaction between  $\text{TiO}_2$  and  $\text{MoS}_2$ .<sup>[12,30]</sup> This result is in good agreement with the TEM observation of lattice distortion in the atomic-scale fused domains, which is also due to lattice stress and the strong interface interaction during the hydrothermal synthesis. This generation of new bonds is the direct reason for the change in the chemical environment of the ele-

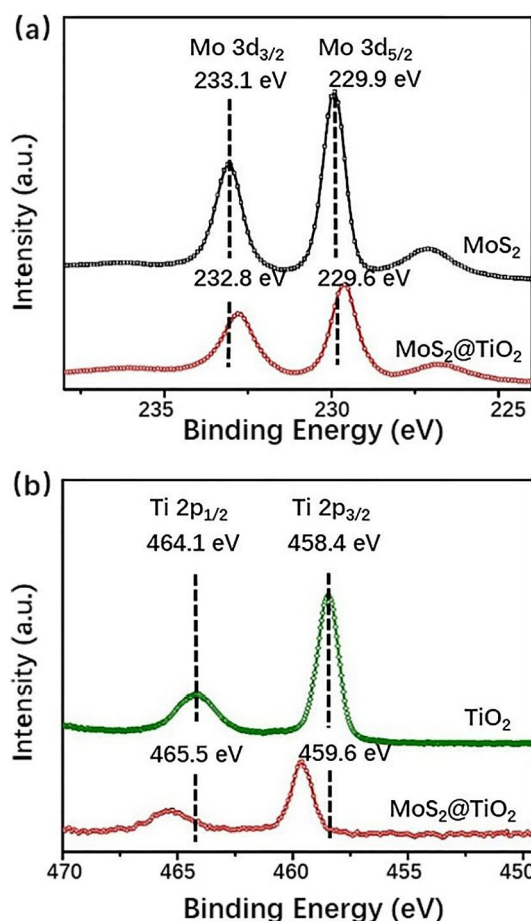


**Figure 5.** High-resolution XPS curves for a) the Mo 3d and b) the Ti 2p regions of  $\text{MoS}_2$ ,  $\text{TiO}_2$ , and  $\text{MoS}_2@\text{TiO}_2$ .

ments, and results in the XPS peak shift. The XPS peak at around 530.1 eV for O 1s (Figure S9b) is ascribed to the formation of Ti-O-Mo bonds between  $\text{MoS}_2$  and  $\text{TiO}_2$ .<sup>[11]</sup> Generally, efficient transfer of the charge carriers across the semiconductor interface is key for photocatalytic efficiency, and the heterostructure is beneficial to the interfacial charge transfer.<sup>[31-33]</sup> Thus the photocatalytic activity can be significantly enhanced.

Figure 6a shows the periodic on/off photocurrent response of all samples under visible light. After a stability pretreatment of 10 cycles (1000 s), the 50th photocurrent cycle showed high stability for  $\text{MoS}_2@\text{TiO}_2$  (which retained 83% of the 10th cycle value). In contrast, the other samples exhibited very poor photocurrent response (Figure 6a, inset). This further confirms that the intimate  $\text{MoS}_2@\text{TiO}_2$  heterojunctions can significantly enhance the photocatalytic activity. The slower decay time implies that photogenerated electrons in the  $\text{MoS}_2@\text{TiO}_2$  nanocomposite can have much longer carrier lifetime than in  $\text{MoS}_2$ .<sup>[34]</sup> Therefore,  $\text{MoS}_2@\text{TiO}_2$  has better photocatalytic performance than  $\text{MoS}_2$  and  $\text{TiO}_2$ . Moreover, the electron transfer between  $\text{MoS}_2$  and  $\text{TiO}_2$  was investigated by using photoluminescence spectroscopy (PL; Figure S10). Normally, the PL signals of semiconductor materials result from the recombination of photoinduced charge carriers. The lower the PL intensity, the lower the recombination rate of photoinduced electron-hole pairs and the higher the photocatalytic activity of the

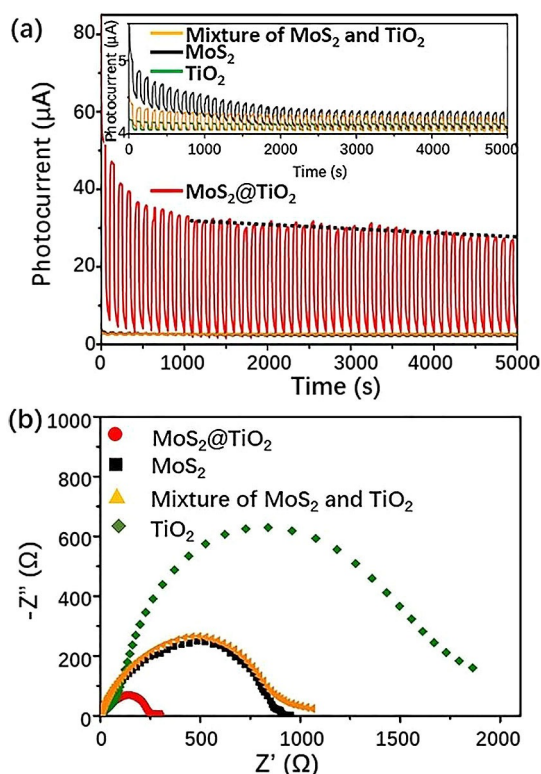


**Figure 6.** a) Transient photocurrent response of MoS<sub>2</sub>@TiO<sub>2</sub> and inset: transient photocurrent responses of MoS<sub>2</sub>, TiO<sub>2</sub>, and a MoS<sub>2</sub> and TiO<sub>2</sub> mixture in aqueous Na<sub>2</sub>SO<sub>4</sub> (0.5 mol L<sup>-1</sup>) at a bias voltage of 0.5 V under visible-light irradiation ( $\lambda \geq 420$  nm). b) EIS plot of the various samples as indicated for the HER process in aqueous H<sub>2</sub>SO<sub>4</sub> (0.5 mol L<sup>-1</sup>).

semiconductor photocatalyst. The PL intensity of pure MoS<sub>2</sub> and MoS<sub>2</sub>@TiO<sub>2</sub> samples revealed a significant decrease after the introduction of TiO<sub>2</sub>. This indicates that MoS<sub>2</sub>@TiO<sub>2</sub> has a relatively low recombination rate of electrons and holes under visible-light irradiation. This is ascribed to the fact that the electrons are excited from the valence band to the conduction band of MoS<sub>2</sub> and then migrate to the TiO<sub>2</sub> nanosheets, which prevents direct recombination of electrons and holes.

Furthermore, the electrochemical impedance spectroscopy (EIS) of MoS<sub>2</sub>, TiO<sub>2</sub>, a mixture of MoS<sub>2</sub> and TiO<sub>2</sub>, and MoS<sub>2</sub>@TiO<sub>2</sub> was studied at the onset potential (Figure 6b). The charge-transfer resistance ( $R_{ct}$ ) of MoS<sub>2</sub>@TiO<sub>2</sub> is 265 Ω, which is much smaller than that of pure MoS<sub>2</sub> (879 Ω). The mixture of MoS<sub>2</sub> and TiO<sub>2</sub> did not show enhancement of the charge transfer owing to the weak interactions between MoS<sub>2</sub> and TiO<sub>2</sub>. When TiO<sub>2</sub> and MoS<sub>2</sub> form heterojunctions, the nanofused interface between TiO<sub>2</sub> and MoS<sub>2</sub> enhances the charge carrier transfer and thus promotes the HER performance.<sup>[18,35,36]</sup> Also, exchange current densities were obtained by applying the extrapolation method to the Tafel plots (Figure S11 and Table S2). As shown in Table S2, MoS<sub>2</sub>@TiO<sub>2</sub> exhibits a remarkable exchange current density ( $j_0$ ) of 25.1 μA cm<sup>-2</sup>, which is about 1.9 times that of pure MoS<sub>2</sub> and suggests excellent activity for HER catalysis. Because the exchange current density is related to electron transfer efficiency, this further indicates enhancement of the charge transfer in our design.

TiO<sub>2</sub> plays two roles in improving electrocatalytic HER performance. First, TiO<sub>2</sub> nanosheets prevent MoS<sub>2</sub> from stacking into multilayers and forming bulk morphology (Figure 2 and Figure S1), which favors the exposure of active sites.<sup>[12]</sup> The density of active sites can be evaluated by the double-layer capacitance.<sup>[37]</sup> The calculated double-layer capacitance was used to evaluate the density of active sites,<sup>[38–41]</sup> which was found to be around 13 times that of pure MoS<sub>2</sub> (Figure S12). This suggests a significant increase in the density of active sites. Second, the formation of heterojunctions between TiO<sub>2</sub> and MoS<sub>2</sub> is beneficial for the efficient electron transport and HER kinetics at the MoS<sub>2</sub>@TiO<sub>2</sub> interface (Figure 6b).<sup>[18,35]</sup>

Figure 7 illustrates the proposed mechanism for photocatalysis and electrocatalysis over MoS<sub>2</sub>@TiO<sub>2</sub>. Figure 7, left, depicts the degradation of organic compounds, such as acetone and

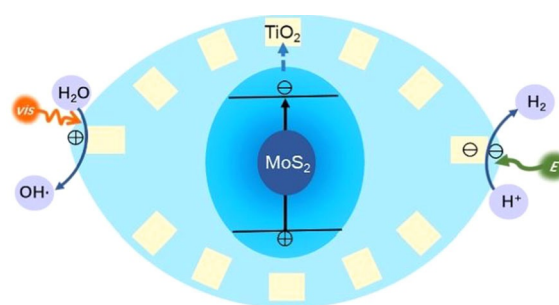


**Figure 7.** Schematic representation of the photocatalytic RhB or acetone degradation reactions under visible-light (vis) irradiation and HER over MoS<sub>2</sub>@TiO<sub>2</sub>.

RhB. With the response of MoS<sub>2</sub>@TiO<sub>2</sub> under visible-light excitation, electrons can migrate from the valence band to the conduction band of MoS<sub>2</sub>. Then the photoinduced electrons can be injected from MoS<sub>2</sub> to the conduction band of TiO<sub>2</sub> because the conduction band of MoS<sub>2</sub> is slightly higher than that of TiO<sub>2</sub> (Figure S13), which thus improves the separation efficiency of the photogenerated electron–hole pairs and enhances the photocatalytic activity. The holes can oxidize water into hydroxyl radicals (·OH) (Figure S14), which are highly oxidative and can react with organic species. The electrocatalytic hydrogen evolution of MoS<sub>2</sub>@TiO<sub>2</sub> is illustrated in Figure 7, right. Similar to the degradation process, electrons can be transferred from MoS<sub>2</sub> to TiO<sub>2</sub>, which facilitates the charge transfer and enhances the electrocatalytic activity.

## Conclusions

In summary, hierarchical MoS<sub>2</sub>@TiO<sub>2</sub> heterojunctions have been successfully synthesized in a one-step hydrothermal method, and exhibit excellent properties in photodegradation and electrocatalytic HER. The enhanced performance may be attributed to two reasons: First, limited aggregation of MoS<sub>2</sub> due to the existence of TiO<sub>2</sub> nanosheets, which consequently maintain the exposure of active sites. Second, the atomic-scale heterojunctions in MoS<sub>2</sub>@TiO<sub>2</sub> favor the efficient transfer of charge carriers and thus promote catalytic activity. This work offers a

promising way to prevent the self-aggregation of MoS<sub>2</sub> and provides new insights for the design of heterojunctions for materials with lattice mismatches.

## Experimental Section

Cesium carbonate (Cs<sub>2</sub>CO<sub>3</sub>; 99%), titanium dioxide (TiO<sub>2</sub>; 98%), hydrogen chloride (HCl; 37%), ammonium molybdate(VI) tetrahydrate ((NH<sub>4</sub>)<sub>6</sub>Mo<sub>7</sub>O<sub>24</sub>·4H<sub>2</sub>O; 99%), and thiourea (CH<sub>4</sub>N<sub>2</sub>S; 99%) were provided by Sinopharm Chemical Reagent Co. Tetrabutylammonium hydroxide (C<sub>16</sub>H<sub>37</sub>NO; ≈ 25% in H<sub>2</sub>O) was provided by Shanghai Aladdin Biochemical Technology Co. All chemical reagents were as received without further purification and distilled water was used in all experiments.

### Synthesis of protonic titanate nanosheets

Layered cesium titanate Cs<sub>2</sub>Ti<sub>2-x/4</sub>□<sub>x/4</sub>O<sub>4</sub> (CTO) was obtained by a solid-state reaction, in which a mixture of Cs<sub>2</sub>CO<sub>3</sub> and TiO<sub>2</sub> (5:3 molar ratio) was heated at 800 °C for 20 h. The corresponding protonic form (HTO) was obtained by treating cesium titanate powder with aqueous 1 M HCl at RT for 3 d.

During the proton exchange reaction, the aqueous HCl was replaced with a fresh solution every 24 h. The layered protonic titanate was exfoliated into single titanate sheets by intercalating TBA (tetrabutyl ammonium) molecules. In a typical reaction, HTO (0.1 g) was added to a mixture of deionized water (24.5 mL) and tetrabutylammonium hydroxide (0.52 mL), then shaken for 7 d.

### Synthesis of MoS<sub>2</sub>

MoS<sub>2</sub> was synthesized through a simple hydrothermal procedure. Ammonium molybdate tetrahydrate (1 mmol) and thiourea (30 mmol) were dissolved in deionized water (25 mL). The mixture was stirred for 30 min, then transferred to a 50 mL Teflon-lined autoclave and heated in an air-flow electric oven at 220 °C for 18 h. After cooling to RT, the samples were obtained by centrifugal separation, washed with water and ethanol five times, and then dried at 60 °C for 12 h.

### Synthesis of MoS<sub>2</sub>@TiO<sub>2</sub> heterojunctions

MoS<sub>2</sub>@TiO<sub>2</sub> heterojunctions were synthesized through a simple hydrothermal procedure. In a typical reaction, ammonium molybdate tetrahydrate and thiourea were dissolved in a suspension of exfoliated titanate nanosheets (25 mL, 4 mg mL<sup>-1</sup>). The mixture was stirred for 30 min, then transferred to a 50 mL Teflon-lined autoclave and heated in an air-flow electric oven at 220 °C for 18 h. After cooling to RT, the samples were collected by centrifugal separation, washed with water and ethanol five times, and then dried at 60 °C for 12 h.

For comparison, different amounts of (NH<sub>4</sub>)<sub>6</sub>Mo<sub>7</sub>O<sub>24</sub>·4H<sub>2</sub>O (0.09, 1.0, 0.11 g) and CH<sub>4</sub>N<sub>2</sub>S (16.51, 1.83, 0.20 g) were used to synthesize the MoS<sub>2</sub>@TiO<sub>2</sub> samples, and the final TiO<sub>2</sub>/MoS<sub>2</sub> weight ratios were about 0.02, 0.11, and 0.75, respectively. The samples were denoted as MoS<sub>2</sub>@TiO<sub>2</sub>-x (x = weight ratio of TiO<sub>2</sub>@MoS<sub>2</sub>).

### Characterization

The morphology of the samples was observed by using a field-emission scanning electron microscope (FESEM, S-4800, HITACHI) and a transmission electron microscope (TEM, JEM2100F). Energy-dispersive X-ray spectroscopy (EDS) elemental mapping images

were performed in combination with SEM. Powder X-ray diffraction (XRD) patterns were recorded by using an X-ray diffractometer with Cu<sub>Kα</sub> radiation (D8 Advance, Bruker, λ = 1.5418 Å). The specific surface area was measured at 77 K by using a Micromeritics ASAP 3020 system. ICP measurements were recorded by using an inductively coupled plasma-atomic emission spectrometer (ICP-AES, Prodigy7). UV/Vis spectra were measured by using a UV/Vis spectrophotometer (UV-2550, Shimadzu, Japan). The photoluminescence spectra (PL) were recorded by using a LS 55 instrument (Perkin-Elmer) with an excitation wavelength of λ = 500 nm. X-ray photoelectron spectroscopy (XPS) measurements were performed by using a PHI Quantera II, (ULVAC-PHI, Japan) for chemical composition analysis, all binding energies were calibrated to the C 1s peak at 284.8 eV.

### Photocatalytic activity evaluation

The photocatalytic activity of the samples was estimated from the degradation of RhB. The catalyst (0.01 g) was dispersed in aqueous RhB (100 mL, 1 × 10<sup>-5</sup> mol) in a beaker, and the distance between the solution and the lamp was fixed at 10 cm (the excitation power density was 80 mW cm<sup>-2</sup>). The suspension was stirred in the dark for 30 min to establish the adsorption/desorption equilibrium between the dye molecules, until the concentration of RhB no longer changed. For the irradiation source, a 300 W xenon lamp (PLS-SXE300, Beijing Trusttech Co.) with a λ = 420 nm cutoff filter was used in the experiment. The absorbance of the solution was recorded by using a UV/Vis absorption photometer (UV-2550, Shimadzu, Japan).

To test the vapor-phase catalysis of the samples, we chose acetone as the pollutant to detect the performance of the samples. In a typical experiment, we added the photocatalyst (10 mg) and ethanol (2 mL) to a glass reactor, sonicated the mixture for 30 min to get a suspension, and then it dried at 40 °C for 12 h. The catalyst was deposited on the bottom of the reactor to form thin films. The reactor was then put into a sealed vessel and acetone (5 μL) was added through an injection valve to form an initial concentration of 600 ppm. We allowed 30 mins to balance the concentration of acetone. For the irradiation source, a 300 W xenon lamp (PLS-SXE300, Beijing Trusttech Co.) with a λ = 420 nm cut-off filter was used in the experiment. Every 10 min, a sample of gas (100 μL) was taken from the system by syringe and analyzed by using a gas chromatograph (Gas Chromatograph GC 900C).

### Electrochemical measurements

The catalyst (5 mg) and 5 wt% Nafion solution (50 μL) were dispersed in isopropanol (950 mL) and sonicated for at least 30 min to form a homogeneous ink. Then 10 μL of the catalyst ink (containing 50 μg of catalyst) was loaded onto a glassy carbon electrode (loading ≈ 0.255 mg cm<sup>-2</sup>). Linear sweep voltammetry (by using the CHI 660D electrochemical workstation from Chenhua Instrument) at a scan rate of 5 mV s<sup>-1</sup> was conducted in 0.5 M H<sub>2</sub>SO<sub>4</sub> with an Ag/AgCl electrode as the reference electrode, a graphite rod as the counter electrode, and the glassy carbon electrode as the working electrode. AC impedance measurements were carried out in the same configuration at η = -0.25 V from 10<sup>5</sup>-0.01 Hz with an AC voltage of 5 mV.

### Photocurrent measurements

Photocurrent tests were carried out in a conventional three-electrode system by using a CHI 660D electrochemical workstation (Chenhua Instrument, Shanghai, China) with Pt foil as the counter

electrode and a Ag/AgCl reference electrode at a 0.5 V potential bias under a PLS-SXE-300C lamp. The working electrodes were prepared by dispersing the catalyst (5 mg) and Nafion solution (100  $\mu$ L, 0.5 wt%) in a water/ethanol mixture (1 mL, 1:1 v/v) and sonicating for at least 30 min to form a homogeneous ink. The working electrode was prepared by drop-casting this ink (50  $\mu$ L) onto FTO glass with an area of 1 cm<sup>2</sup>

### Analysis of hydroxyl radicals ( $\cdot$ OH)

The formation of hydroxyl radicals ( $\cdot$ OH) on the surface of visible-light-irradiated MoS<sub>2</sub>@TiO<sub>2</sub> can be detected by using terephthalic acid as a probe molecule. Terephthalic acid can react with  $\cdot$ OH and produce a fluorescent hydroxy product, 2-hydroxyterephthalic acid. The PL intensity at about  $\lambda = 425$  nm gradually increased as the irradiation time was prolonged, which indicated the gradual accumulation of  $\cdot$ OH.<sup>[42,43]</sup> In a typical experiment, the catalyst (5 mg) was added to an aqueous solution of terephthalic acid (3 mM) and NaOH (10 mM), and the suspension was stirred in the dark for 30 min. For the irradiation source, a 300 W xenon lamp (PLS-SXE300, Beijing Trusttech Co.) with a  $\lambda = 420$  nm cutoff filter was used. After irradiation with visible light, the reaction solution was collected every 15 min to measure the PL intensity at  $\lambda = 425$  nm (excited at  $\lambda = 315$  nm).

### Acknowledgements

This work was supported by the National Key R&D Program of China (2017YFC1103800), PCSIRT (IRT 15R52), NSFC (U1662134, U1663225, 51472190, 51611530672, 51503166, 21706199, 21711530705), ISTCP (2015DFE52870), HPNSF (2016CFA033, 2017CFB487), and SKLPPC (PPC2016007).

### Conflict of interest

The authors declare no conflict of interest.

**Keywords:** electrochemistry · hybrid structures · hydrogen · nanostructures · photochemistry

- [1] D. Voiry, M. Salehi, R. Silva, T. Fujita, M. Chen, T. Asefa, V. B. Shenoy, G. Eda, M. Chhowalla, *Nano. Lett.* **2013**, *13*, 6222–6227.
- [2] J. Chen, N. Kuriyama, H.-T. Yuan, H. Takeshita, T. Sakai, *J. Am. Chem. Soc.* **2001**, *123*, 11813–11814.
- [3] O. Lopez-Sanchez, D. Lembke, M. Kayci, A. Radenovic, A. Kis, *Nat. Nanotechnol.* **2013**, *8*, 497–501.
- [4] M. Shen, Z. Yan, L. Yang, P. Du, J. Zhang, B. Xiang, *Chem. Commun.* **2014**, *50*, 15447–15449.
- [5] F. Meng, J. Li, S. K. Cushing, M. Zhi, N. Wu, *J. Am. Chem. Soc.* **2013**, *135*, 10286–10289.
- [6] B. Luo, G. Liu, L. Wang, *Nanoscale* **2016**, *8*, 6904–6920.
- [7] B. Chen, Y.-H. Meng, J.-W. Sha, C. Zhong, W.-B. Hu, N.-Q. Zha, *Nanoscale* **2018**, *10*, 34–68.
- [8] J. Liu, Y. Li, J. Ke, Z. Wang, H.-N. Xiao, *Catalysts* **2017**, *7*, 30.
- [9] L. Zheng, S. Han, H. Liu, P. Yu, X. Fang, *Small* **2016**, *12*, 1527–1536.
- [10] X. Zhu, C. Yang, F. Xiao, J. Wang, X. Su, *New J. Chem.* **2015**, *39*, 683–688.
- [11] C. Liu, L. Wang, Y. Tang, S. Luo, Y. Liu, S. Zhang, Y. Zeng, Y. Xu, *Appl. Catal. B* **2015**, *164*, 1–9.
- [12] L. Guo, Z. Yang, K. Marcus, Z. Li, B. Luo, L. Zhou, X. Wang, Y. Du, Y. Yang, *Energy Environ. Sci.* **2018**, *11*, 106–114.
- [13] H. Fu, K. Yu, H. Li, J. Li, B. Guo, Y. Tan, C. Song, Z. Zhu, *Dalton Trans.* **2015**, *44*, 1664–1672.
- [14] J. Wang, B. Wei, L. Xu, H. Gao, W. Sun, J. Che, *Mater. Lett.* **2016**, *179*, 42–46.
- [15] W. Ren, W. Zhou, H. Zhang, C. Cheng, *ACS Appl. Mater. Interfaces* **2017**, *9*, 487–495.
- [16] C. Meng, Z. Liu, T. Zhang, J. Zhai, *Green Chem.* **2015**, *17*, 2764–2768.
- [17] R. Dai, A. Zhang, Z. Pan, A. M. Al-Enizi, A. A. Elzatahry, L. Hu, G. Zheng, *Small* **2016**, *12*, 2792–2799.
- [18] B. Ma, P. Y. Guan, Q. Y. Li, M. Zhang, S. Q. Zang, *ACS Appl. Mater. Interfaces* **2016**, *8*, 26794–26800.
- [19] Y. Lu, X. Cheng, G. Tian, H. Zhao, L. He, J. Hu, S.-M. Wu, Y. Dong, G.-G. Chang, S. Lenaerts, S. Siffert, G. Van Tendeloo, Z.-F. Li, L.-L. Xu, X.-Y. Yang, B.-L. Su, *Nano Energy* **2018**, *47*, 8–17.
- [20] T. Sasaki, M. Watanabe, *J. Am. Chem. Soc.* **1998**, *120*, 4682–4689.
- [21] P.-H. Wen, Y. Ishikawa, H. Itoh, Q. Feng, *J. Phys. Chem. C* **2009**, *113*, 20275–20280.
- [22] P.-H. Wen, H. Itoh, W.-P. Tang, Q. Feng, *Langmuir* **2007**, *23*, 11782–11790.
- [23] K. Zhu, G. Hu, J. Supercrit, *Fluids* **2014**, *94*, 165–173.
- [24] N. Jiang, X.-Y. Yang, G.-L. Ying, L. Shen, J. Liu, W. Geng, L. J. Dai, S. Y. Liu, J. Cao, G. Tian, T. L. Sun, S. P. Li, B.-L. Su, *Chem. Sci.* **2015**, *6*, 486–491.
- [25] N. Jiang, X.-Y. Yang, Z. Deng, L. Wang, Z. Y. Hu, G. Tian, G. L. Ying, L. Shen, M. X. Zhang, B.-L. Su, *Small* **2015**, *11*, 2003–2010.
- [26] X.-Y. Yang, L.-H. Chen, Y. Li, J. C. Rooke, C. Sanchez, B.-L. Su, *Chem. Soc. Rev.* **2017**, *46*, 481–558.
- [27] B. Lim, M. Jiang, P. H. Camargo, E. C. Cho, J. Tao, X. Lu, Y. Zhu, Y. Xia, *Science* **2009**, *324*, 1302–1305.
- [28] X.-F. Li, T.-X. Fan, H. Zhou, S.-K. Chow, W. Zhang, D. Zhang, Q.-X. Guo, H. Ogawa, *Adv. Funct. Mater.* **2009**, *19*, 45–56.
- [29] J. Xie, J. Zhang, S. Li, F. Grote, X. Zhang, H. Zhang, R. Wang, Y. Lei, B. Pan, Y. Xie, *J. Am. Chem. Soc.* **2013**, *135*, 17881–17888.
- [30] W. Zhou, Z. Yin, Y. Du, X. Huang, Z. Zeng, Z. Fan, H. Liu, J. Wang, H. Zhang, *Small* **2013**, *9*, 140–147.
- [31] Z. Lu, L. Zeng, W. Song, Z. Qin, D. Zeng, C. Xie, *Appl. Catal. B* **2017**, *202*, 489–499.
- [32] H. Zhou, L. Ding, T.-X. Fan, J. Ding, D. Zhang, Q.-X. Guo, *Appl. Catal. B* **2014**, *147*, 221–228.
- [33] L.-Q. Wu, L.-H. Hao, B. Pang, G.-F. Wang, Y. Zhang, X.-H. Li, *J. Mater. Chem. A* **2017**, *5*, 4629–4637.
- [34] H. Han, K. M. Kim, C. W. Lee, C. S. Lee, R. C. Pawar, J. L. Jones, Y. R. Hong, J. H. Ryu, T. Song, S. H. Kang, H. Choi, S. Mhin, *Phys. Chem. Chem. Phys.* **2017**, *19*, 28207–28215.
- [35] Y. Shen, X. Ren, X. Qi, J. Zhou, Z. Huang, J. Zhong, *J. Electrochem. Soc.* **2016**, *163*, H1087–H1090.
- [36] X. Song, G. Chen, L. Guan, H. Zhang, J. Tao, *Appl. Phys. Express* **2016**, *9*, 095801.
- [37] A. P. Murthy, J. Theerthagiri, J. Madhavan, K. Murugan, *Phys. Chem. Chem. Phys.* **2017**, *19*, 1988–1998.
- [38] L. Ma, Y. Hu, G. Zhu, R. Chen, H. Lu, Y. Wang, J. Liang, H. Liu, C. Yan, Z. Tie, Z. Jin, J. Liu, *Chem. Mater.* **2016**, *28*, 5733–5742.
- [39] J. Liang, C. Wang, P. Zhao, Y. Wang, L. Ma, G. Zhu, Y. Hu, Z. Lu, Z. Xu, Y. Ma, T. Chen, Z. Tie, J. Liu, Z. Jin, *ACS Appl. Mater. Interfaces* **2018**, *10*, 6084–6089.
- [40] J. D. Benck, Z. Chen, L. Y. Kuritzky, A. J. Forman, T. F. Jaramillo, *ACS Catal.* **2012**, *2*, 1916–1923.
- [41] M. A. Lukowski, A. S. Daniel, F. Meng, A. Forticaux, L. Li, S. Jin, *J. Am. Chem. Soc.* **2013**, *135*, 10274–10277.
- [42] K. Ishibashi, A. Fujishima, T. Watanabe, K. Hashimoto, *Electrochem. Commun.* **2000**, *2*, 207–210.
- [43] J.-G. Yu, W.-G. Wang, B. Cheng, B.-L. Su, *J. Phys. Chem. C* **2009**, *113*, 6743–6750.

Manuscript received: March 11, 2018

Revised manuscript received: April 1, 2018

Accepted manuscript online: April 10, 2018

Version of record online: May 18, 2018